Instrument Science Report WFC3 2016-08

WFC3/UVIS Dark Calibration: Monitoring Results and Improvements to Dark Reference Files

M. Bourque & S. Baggett

April 22, 2016

Abstract

The Wide Field Camera 3 (WFC3) UVIS detector possesses an intrinsic signal during exposures, even in the absence of light, known as dark current. A daily monitor program is employed every HST cycle to characterize and measure this current as well as to create calibration files which serve to subtract the dark current from science data. We summarize the results of the daily monitor program for all on-orbit data. We also introduce a new algorithm for generating the dark reference files that provides several improvements to their overall quality. Key features to the new algorithm include correcting the dark frames for Charge Transfer Efficiency (CTE) losses, using an anneal-cycle average value to measure the dark current, and generating reference files on a daily basis. This new algorithm is part of the release of the CALWF3 v3.3 calibration pipeline on February 23, 2016 (also known as "UVIS 2.0"). Improved dark reference files have been regenerated and re-delivered to the Calibration Reference Data System (CRDS) for all on-orbit data. Observers with science data taken prior to the release of CALWF3 v3.3 may request their data through the Mikulski Archive for Space Telescopes (MAST) to obtain the improved products.

Introduction

The Wide Field Camera 3 (WFC3) UVIS CCD detector exhibits an intrinsic, non-zero count rate in all exposures, including those in which the shutter remains closed. Known

as *dark current*, this signal is present in all WFC3/UVIS observations and thus must be corrected before scientific analysis can occur. To perform this calibration, HST programs are employed every proposal cycle to collect UVIS dark images on a daily basis and characterize the behavior of the dark current. The data are then used to generate dark reference files that in turn are used in the WFC3 calibration pipeline (CALWF3) to subtract the dark current from science images. Additionally, the daily acquisition of UVIS darks serves as a monitor of the health and stability of the UVIS CCD detector over time, providing a means to measure the effects of radiation damage sustained on-orbit.

There are several distinct populations of pixels within a typical UVIS dark image: (1) a uniform background of low count-rate pixels (currently ∼8 e-/hr), (2) individual pixels that have a high dark current, known as *hot pixels* (defined as >54 e-/hr), and (3) groups of pixels that suffer from incident cosmic rays. Figure 1 displays a zoomed-in region of a typical dark image, showing these populations. The 54 e-/hr threshold was chosen for hot pixels based on the tail of a dark histogram generated from data taken early in the mission (see Figure 5.1 of the WFC3 Data Handbook, Deustua et al., 2016, page 96).

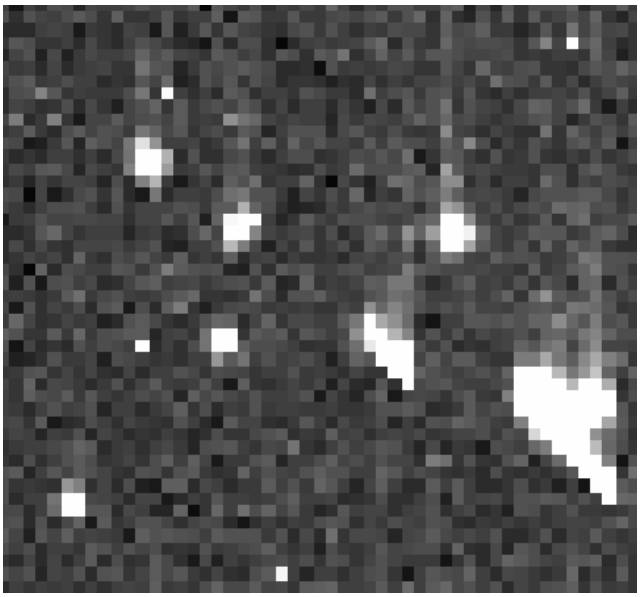

Fig. 1.—*A 50x50 pixel region taken from a 900-second UVIS dark (dataset icqa1mcvq) showing the nominal features of background dark current, hot pixels, and cosmic rays. Image scaling is +/- 5% about the mean.*

The pixel populations can be seen further in Figure 2, which displays a histogram of the distribution of pixel values in a typical 900-second dark image. The left panel shows the distribution covering the uniform background population. Shaded in red are pixels with values exceeding the 54 e-/hr threshold (which corresponds to 13.5 e- in this 900-second image). The right panel displays the tail of the distribution, ranging from 40 to 1000 e-, showing that the image is also comprised of hot pixels and cosmic rays of varying intensity.

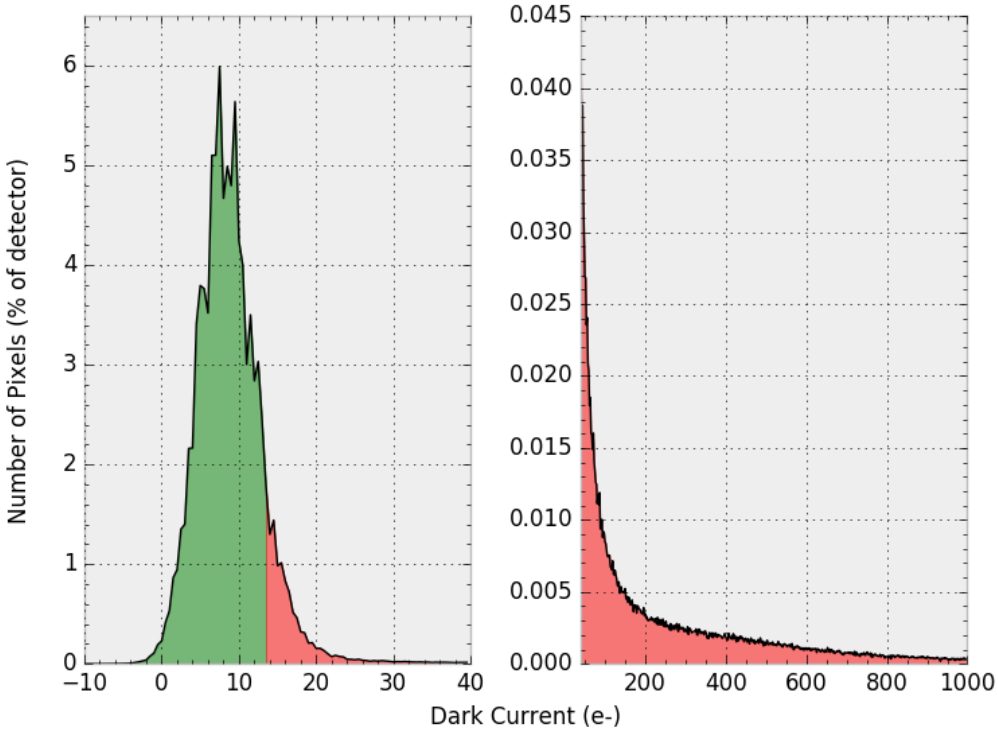

Fig. 2.—*The distribution of pixel values (in electrons) in a 900-second UVIS dark (dataset icqa1mcvq). The pixels with values exceeding the 54 e-/hr threshold (corresponding to 13.5 e- in this image) are shaded in red. The right panel is a zoomed-in display of the tail of the distribution. Bin sizes are 0.5 e- (left) and 1.92 e- (right).*

Additionally, these populations exhibit Charge Transfer Efficiency (CTE) losses, in which signal becomes trapped in neighboring pixels during readout, causing tails of signal in the direction of the readout amplifiers. CTE losses are greater for signals that traverse many pixels during readout, while CTE losses are minimal for pixels close to the readout amplifiers. This effect is shown in Figure 3. Fortunately, CTE losses in dark frames can be mitigated by two means: (1) postflashing, in which the UVIS internal tungsten lamp is turned on during the dark observation, introducing a uniform 12 e- background that helps release charge traps (Biretta and Baggett, 2013) and (2) an empirical pixel-based CTE correction, which has recently been introduced in the CALWF3 v3.3 pipeline (Ryan, R. et al., 2016). Figure 4 shows an example of how these two mitigation options affect a typical cosmic ray; note that CTE losses are nearly non-existent for CTE-corrected, postflashed signal.

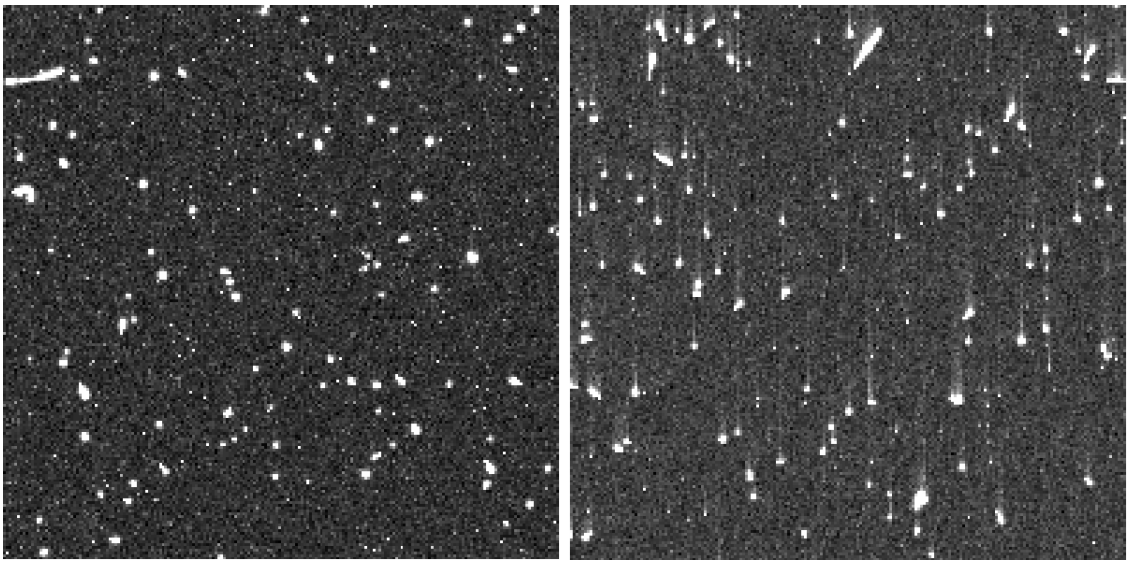

Fig. 3.—*Two 200x200 pixel regions taken from a 900-second UVIS dark (dataset icqa1mcvq), one located close to readout amplifier C (left) and one located far from readout amplifier C (right), showing that CTE losses are more significant further from the readout. The readout amplifier is towards the lower left corner of each image. Image scaling is +/- 5% about the mean.*

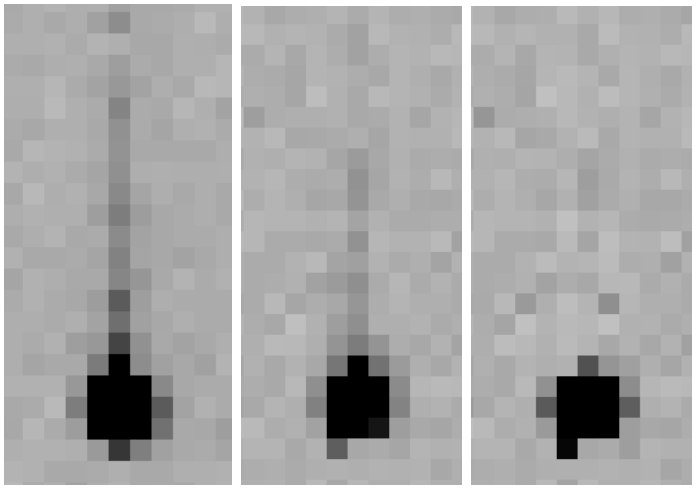

Fig. 4.—*An example of a cosmic ray in a nominal 900s UVIS dark (left), a 900s 12 e- postflashed dark, and a 900s 12 e- postflashed & CTE-corrected dark (right), showing the beneficial effect that the postflashing and CTE correction has on signal trails caused by CTE losses. Note that the direction of readout is down. Image scaling is +/- 5% about the mean.*

The radiation environment in the low-earth orbit in which HST resides degrades the silicon lattice of the UVIS detector over time, resulting in the formation of charge traps and an overall increase in the number of hot pixels. Consequently, roughly 1000 new hot pixels appear each day. However, the WFC3 anneal procedure, in which the UVIS detector

is warmed to ∼20C, helps to expunge some of the charge traps and successfully erases a significant amount of the hot pixels (currently ∼10-20% each anneal). The anneal procedure is performed approximately every four weeks. Figure 5 shows the number of hot pixels present in individual full-frame UVIS dark exposures over time, spanning a typical anneal procedure (February 2011). We see that the number of hot pixels increase by ∼0.3% of the detector over each anneal cycle, and the anneal procedure corrected ∼40% of the hot pixels.

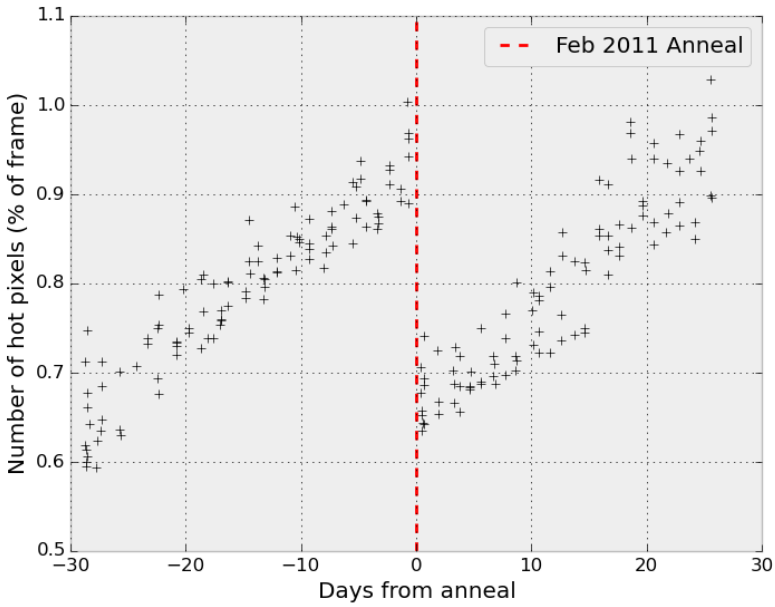

Fig. 5.—*The number of hot pixels in full-frame UVIS dark images over time, spanning the January 2011 and February 2011 anneal cycles.*

This paper discusses the characteristics and results of the UVIS dark calibration for all on-orbit data, as well as some newly implemented calibration techniques that improve the overall quality of the reference files. We first discuss the annual calibration programs that acquire UVIS dark observations. We then characterize the evolution of dark current and hot pixels since WFC3 was first installed on HST in May 2009. Next, we outline an improved algorithm for making UVIS dark reference files and describe its differences from the previous algorithm. Finally, we discuss the delivery of improved dark reference files to the Calibration Reference Data System (CRDS).

Observations

Since WFC3 began taking on-orbit observations in June 2009, calibration programs have been employed each HST proposal cycle to acquire full-frame 900-second UVIS dark

Program ID	Program Title	PI	Cycle	Date Span
11905	WFC3 UVIS CCD Daily Monitor	T. Borders	17	2009-08-10 - 2010-11-01
11909	UVIS Hot Pixel Anneal	S. Baggett	17	2009-08-20 - 2010-10-16
12342	WFC3 UVIS CCD Daily Monitor	T. Borders	18	2010-11-03 - 2011-11-01
12343	UVIS Hot Pixel Anneal	S. Baggett	18	2010-11-13 - 2011-09-18
12687	WFC3/UVIS Anneal	S. Baggett	19	2011-10-14 - 2012-09-12
13103	WFC3/UVIS Anneal	S. Baggett	19	2012-10-11 - 2012-10-12
12689	WFC3 UVIS CCD Daily Monitor	T. Borders	19	2011-11-02 - 2012-11-03
13071	WFC3/UVIS Anneal	S. Baggett	20	2012-11-07 - 2013-10-11
13073	UVIS CCD Daily Monitor A	J. Biretta	20	2012-11-04 - 2013-01-09
13074	UVIS CCD Daily Monitor B	J. Biretta	20	2013-01-10 - 2013-03-16
13075	UVIS CCD Daily Monitor C	J. Biretta	20	2013-03-17 - 2013-07-19
13076	UVIS CCD Daily Monitor D	J. Biretta	20	2013-07-20 - 2013-10-31
13554	WFC3 UVIS Anneal	S. Baggett	21	2013-11-09 - 2014-11-06
13556	UVIS CCD Daily Monitor A	M. Bourque	21	2013-11-02 - 2014-02-23
13557	UVIS CCD Daily Monitor B	M. Bourque	21	2014-02-24 - 2014-06-18
13558	UVIS CCD Daily Monitor C	M. Bourque	21	2014-06-18 - 2014-11-04
14000	WFC3 UVIS Anneal	S. Baggett	22	2014-12-04 - 2015-10-06
14002	WFC3 UVIS Daily Monitor A	M. Bourque	22	2014-11-05 - 2015-03-05
14003	WFC3 UVIS Daily Monitor B	M. Bourque	22	2015-03-06 - 2015-07-04
14004	WFC3 UVIS Daily Monitor C	M. Bourque	22	2015-07-05 - 2015-11-01
14366	WFC3 UVIS Anneal	S. Baggett	23	2015-11-02 - 2016-12-09
14368	WFC3 UVIS Daily Monitor A	M. Bourque	23	2015-11-02 - 2016-03-05
14369	WFC3 UVIS Daily Monitor B	M. Bourque	23	2016-03-06 - 2016-07-05
14370	WFC3 UVIS Daily Monitor C	M. Bourque	23	2016-07-05 - 2016-11-03

Table 1: *WFC3/UVIS calibration programs which acquire UVIS dark exposures that are used for dark reference file generation and UVIS health & stability monitoring. Not listed are the two programs which acquired dark exposures during Servicing Mission Observatory Verification (SMOV): 11431 ("UVIS Hot Pixel Anneal", PI S. Baggett) and 11446 ("WFC3 UVIS dark current, readnoise, and CTE", PI S. Baggett). We did not use data from these programs for the analysis described in this document.*

exposures on a regular basis.[1] Each of these programs are listed in Table 1. Due to a large number of visits, particularly in more recent proposals, programs for some cycles are broken into three separate proposals covering ∼4 months each to facilitate processing and scheduling.

For the UVIS anneal programs (i.e. 11909, 12343, 12687, 13103, 13071, 13554, 14000, and 14366), ten 900-second darks are acquired during each anneal (five immediately prior to and five immediately following the anneal procedure) as a monitor of the success of the procedure. For the CCD Daily Monitor programs, the observations are structured in such a way as to acquire full-frame 900-second UVIS darks (in addition to biases) on a daily basis and thus serving as a daily monitor of the health and stability of the UVIS detector. The program structure has evolved over the lifetime of WFC3; we provide a breakdown of the structure of each program in Appendix A.

The 900-second exposure time for UVIS dark observations was chosen for two reasons: (1) since the UVIS dark current scales linearly with increasing exposure time (reference), one exposure time is used to generate dark reference files to calibrate science observations with various exposure times. (2) During Servicing Mission Observatory Verification (SMOV) (Programs 11431 and 11446), 1800-second dark observations were acquired, but scheduling restrictions and difficulties in cosmic ray rejection led to the decision to break the exposures into two 900-second exposures. For consistency, the 900-second exposure time has been used for all post-SMOV UVIS dark observations.

UVIS Anneal and UVIS CCD Daily Monitor programs are expected to be conducted throughout the remainder of the lifetime of WFC3/UVIS.

Monitoring Results

The UVIS dark frames that are acquired through the anneal and daily monitoring programs are used to monitor the evolution of dark current and hot pixels over time. These monitoring results are shown in Figure 6, which plots the median dark current and the number of hot pixels in each individual dark frame over the ∼7 year on-orbit lifetime of WFC3. The median dark current is measured by taking the median value of all non-hot pixels (i.e. those that have values less than the 54 e-/hr threshold) that are unaffected by cosmic rays. Similarly, the number of hot pixels is counted by summing all of the individual hot pixels (i.e. those that exceed the 54 e-/hr threshold) that are unaffected by cosmic rays.

Figure 6 illustrates the effect that postflash has on the dark current and hot pixel

[1]Full-frame darks are also used to calibrate subarray observations; the CALWF3 calibration pipeline will extract and use the appropriate subarray region in the full-frame dark reference file during dark subtraction.

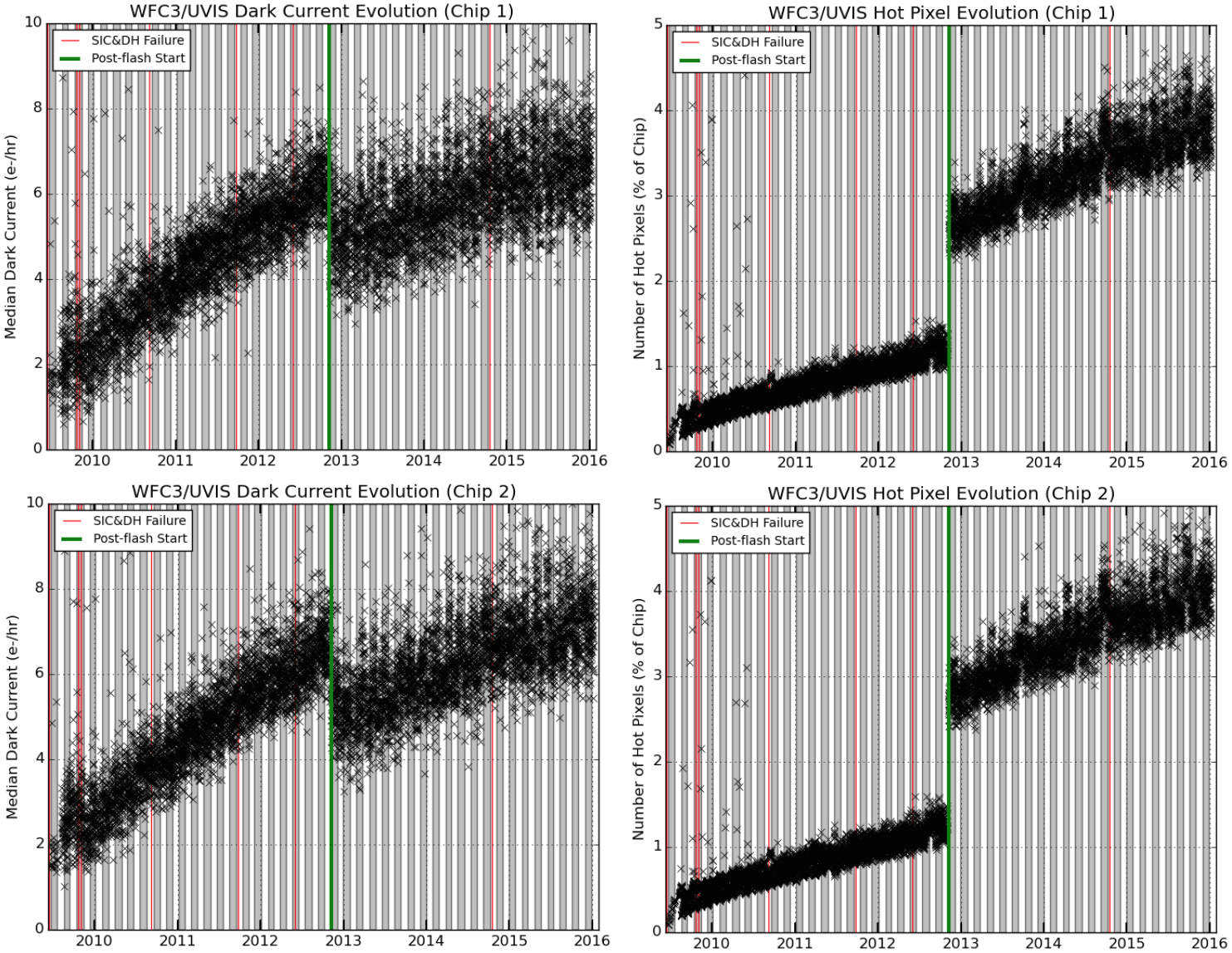

Fig. 6.—*The median dark current (left) and the number of hot pixels (right) over time for UVIS chip 1 (top) and UVIS chip 2 (bottom). Anneal cycles are shaded in gray/white intervals (i.e. gray/white boundaries represent anneal procedures). Science Instrument Control and Data Handling Unit (SIC&DH) failures, in which the UVIS detector may have been warmed, are plotted in red. The postflash start date of November 08, 2012 is plotted in green.*

measurements. Starting with the November 08, 2012 anneal, UVIS dark observations were taken with 12 e- postflash; as previously mentioned, postflashing helps to preserve signal in the cosmic rays and hot pixels that is normally lost to CTE effects (further discussion of postflashing and its effects on UVIS dark observations can be found in Biretta and Bourque, 2014). Thus, postflash allows for measurement of hot pixels and cosmic rays that otherwise would have been difficult to detect. As a result, postflashing leads to an increased number of detected hot pixels and, as seen in the sudden ∼1.5% jump in Figure 6. Postflashing has the opposite effect on dark current; since CTE trails are not as prevalent in postflash observations, they do not have as much of a significant contribution to the dark current measurement, resulting in a decrease in the overall median dark current, as seen in the ∼1 e-/hr drop in Figure 6.

Another characteristic of the monitoring is that there are several anneal cycles (namely the 08/2012, 09/2013, 05/2013, 09/2014, and 09/2015 anneal cycles) in which the number of hot pixels at the beginning of the anneal cycle is 0.5% higher than expected. The first such event was investigated in detail (Baggett et al., 2013). In that case, the standard internal exposures acquired immediately after the Aug 2012 anneal procedure exhibited a higher-than-expected number of hot pixels and also showed evidence for low-level quantum efficiency offsets, known as hysteresis. The cause for the latter was attributed to a power cycle of an electronics box while the detector was cold, behavior which had been noted during ground testing (and as discussed in the report, the hysteresis was successfully neutralized as part of the standard post-anneal procedures so no science data were adversely affected). The additional hot pixels were determined to be unrelated to the hysteresis. Rather, the detector cooldown period for the Aug 2012 anneal was found to have overlapped with a South Atlantic Anomaly passage (SAA, an area known for higher radiation levels). But despite the auspicious coincidence of higher-than-normal hot pixels and an SAA passage, the correlation did not hold up in subsequent high hot pixel events. No alternative cause (e.g. procedural, electronic, etc.) has been identified.

In this study, we extend the analysis of the atypical hot pixel events. First, we plot the number of hot pixels over time for the anomalous anneal cycles as well as several nominal anneal cycles in Figure 7. We see mixed behavior; for some anomalous anneal cycles, (namely the 09/2013, 05/2014, and 09/2014 anneal cycles), the slope of the number of hot pixels is near zero or negative, while other anomalous anneal cycles, (namely the 08/2012 and 09/2015 anneal cycles) exhibit the positive trend that we see in the nominal anneal cycles (e.g. 08/2013, 02/2014).

As an additional check, we analyzed the locations of the hot pixels in order to identify any spatial trends that may be occurring in the anomalous anneal cycles. The results are shown in Figure 8, which plots 100x100 binned full-frame images of aggregate stacks of data quality arrays for every dark observation occurring in anneal cycles, ranging from the 01/2013 anneal to present. In other words, the value of each pixel in Figure 8 represents

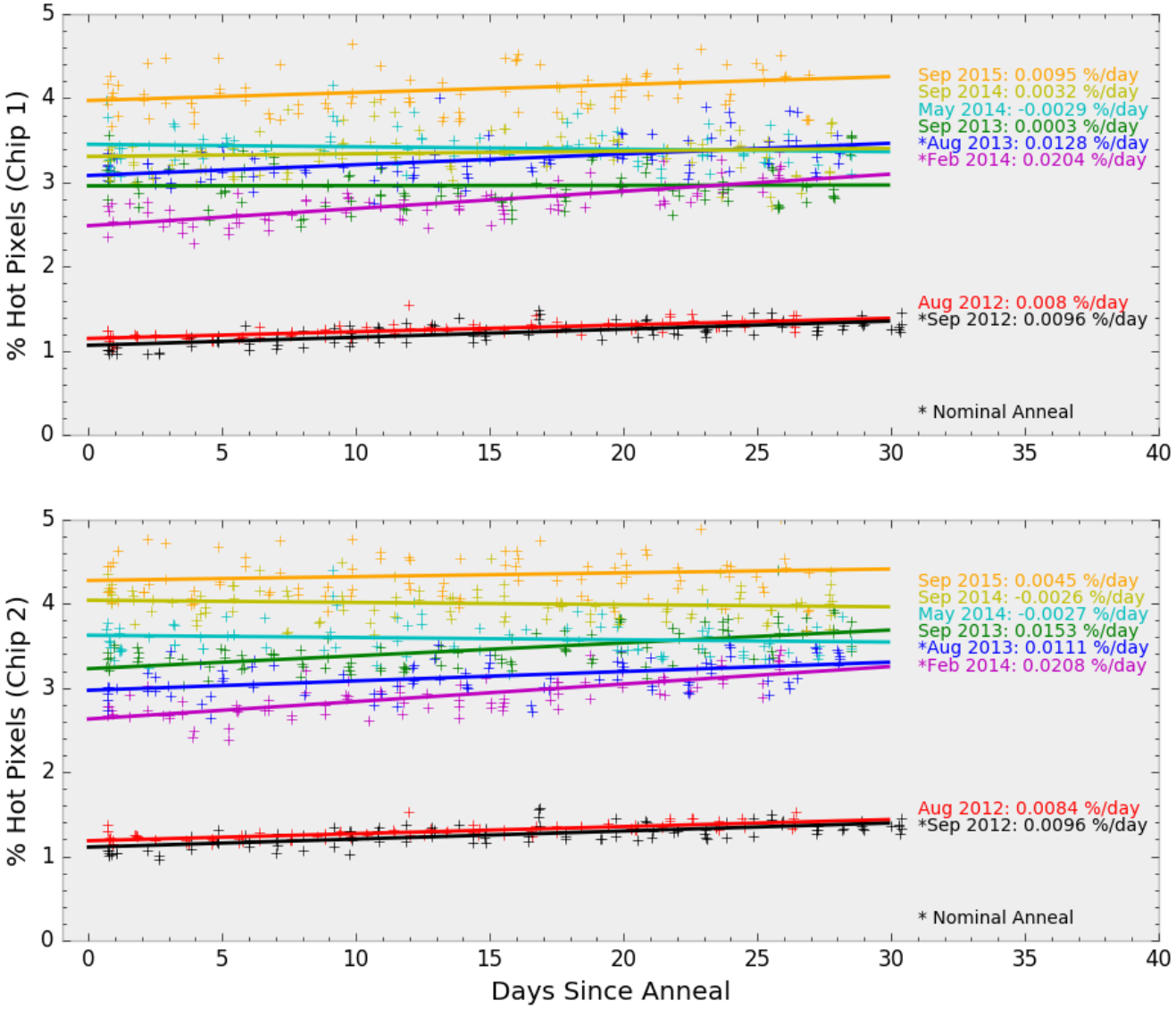

Fig. 7.—*The number of hot pixels over an anneal cycle for several anomalous and nominal anneal cycles for UVIS chip 1 (top) and UVIS chip 2 (bottom). An asterisk denotes a nominal anneal cycle (i.e. no increased amount of hot pixels), while the others represent anomalous anneal cycles (i.e. a non-expected increase in the number of hot pixels). Note that the data occurring in the 2013-2015 epochs are postflashed, and thus generally contain ∼2-3% more hot pixels than the non-postflashed data from 2012 (See Figure 6).*

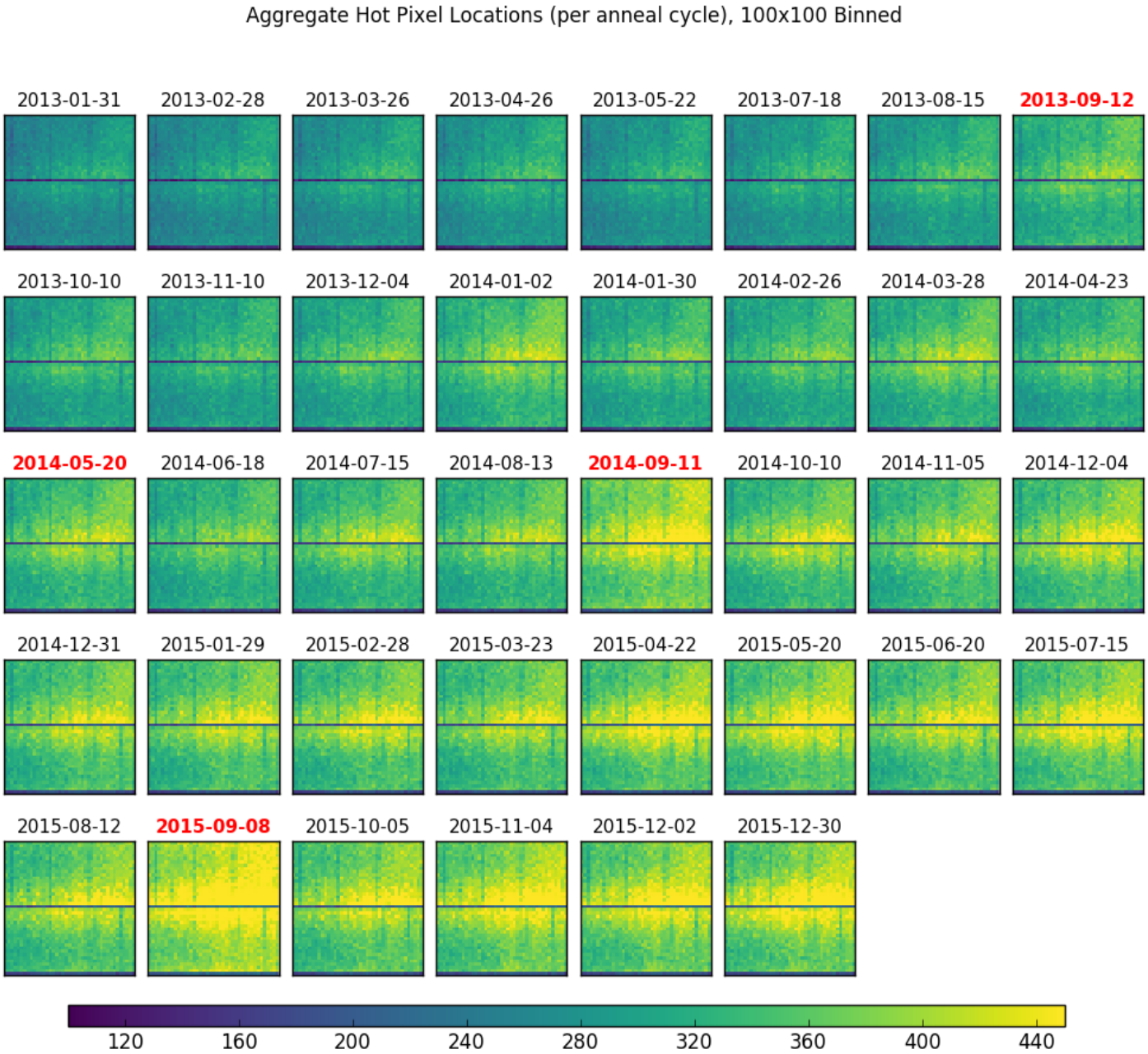

Fig. 8.—*100x100 binned full-frame images of anneal-cycle aggregate hot pixels. Anomalous anneal cycles are labeled in red.*

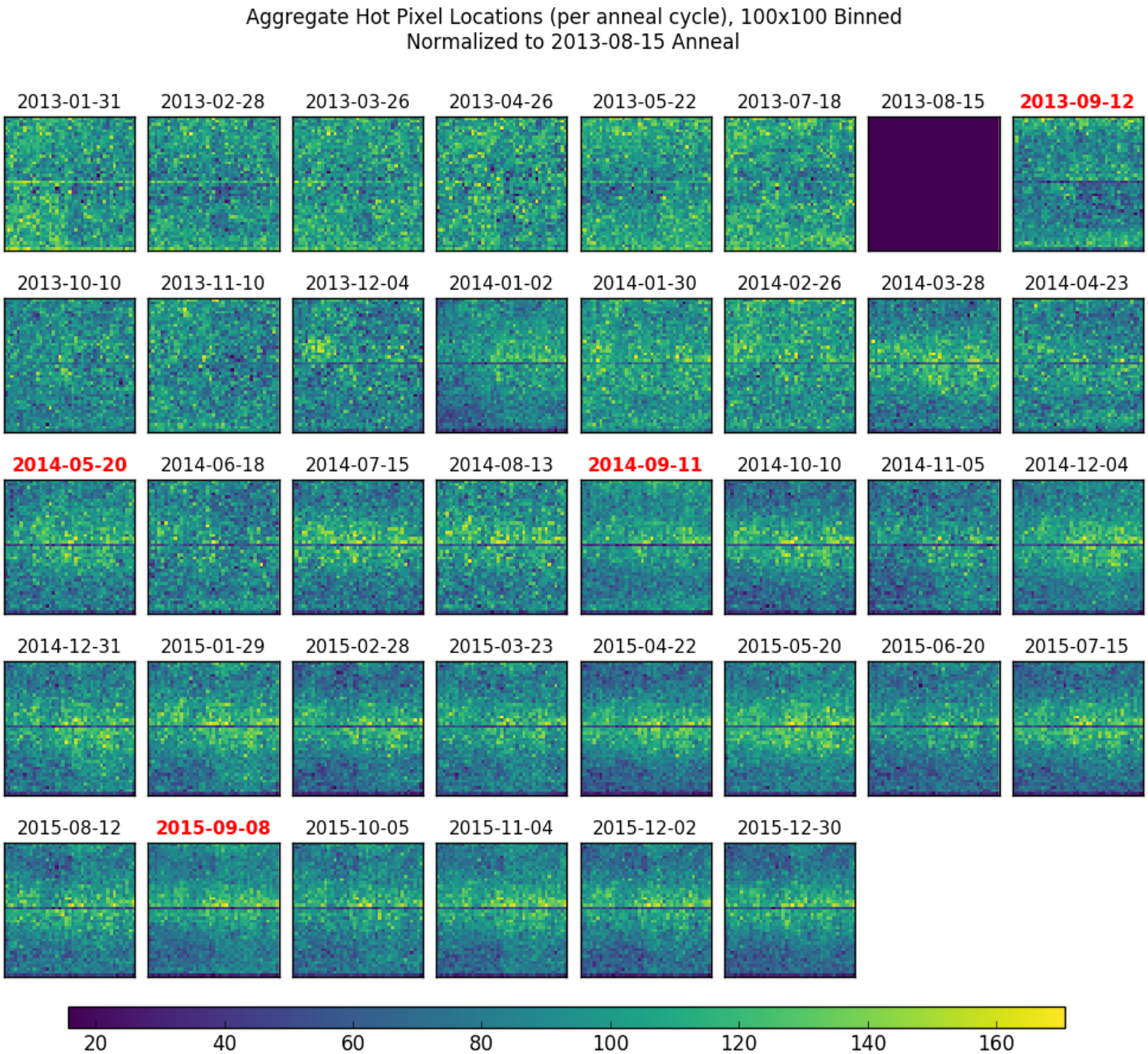

Fig. 9.—*100x100 binned full-frame images of anneal-cycle aggregate hot pixels, normalized to the 2013-08-15 anneal cycle. Anomalous anneal cycles are labeled in red.*

the number of hot pixels that occurred within the 100X100 bin during the particular anneal cycle. We see that, although the anomalous anneal cycles do contain more hot pixels (as expected based on the previous results mentioned), no spatial trends are apparent; for both anomalous and nominal anneal cycles, most of the hot pixels appear to reside near the chip gap, with slight preference towards amplifiers B and D. Furthermore, Figure 9 contains the same stacks normalized to the 2013-08-15 anneal cycle stack (i.e. the 2013-08-15 anneal stack is subtracted from each stack), in attempt to subtract out the underlying spatial pattern exhibited in each stack and potentially reveal spatial trends not otherwise seen. However, again we see no evidence that the anomalous anneals exhibit any particularly odd spatial patterns.

Though the results shown in Figures 7 and 8 show that these anomalous anneal cycles indeed exhibit more hot pixels than normal, the cause remains unknown.

For both pre-postflash and postflash epochs, we see from Figure 6 that the median dark current and the number of hot pixels exhibit a steady increase over time. While overall the behavior appears to be linear, there does seem to be a slight flattening of the trends in 2016-2016. A likely cause – changes in solar activity – could not be conclusively linked to those changes. Our investigation on this matter is discussed in Appendix B.

WFC3/UVIS dark current and hot pixel monitoring will continue through and beyond HST cycle 23.

Improved algorithm

The "UVIS 2.0" update, which is an update to the WFC3/UVIS calibration pipeline available in CALWF3 v3.3, introduces an improved algorithm for the creation of UVIS dark reference files. There are three major changes to the algorithm:

1. *Correcting dark frames for Charge Transfer Efficiency (CTE) losses* - The individual dark frames used to create dark reference files are CTE corrected using a pixel-based empirical CTE correction (Anderson, 2013).

2. *Setting the dark current to an anneal-cycle average value* - Instead of setting non-hot pixels (i.e. pixels with values below the 54 e-/hr threshold) to the median value of the "superdark", each non-hot pixel is set to its corresponding "masterdark" value, where the "masterdark" is an average of all individual dark frames from an entire anneal cycle.

3. *Generating dark reference files on a daily basis* - Instead of using a hard 4-day window of individual dark frames to create superdarks, (i.e. superdark 1 is from frames acquired during days 1-4 of the anneal cycle, superdark 2 from days 4-8, superdark 3 from days 8-12, etc.), a sliding 4-day window is used (i.e. superdark 1 from days 1-4, superdark 2 from days 2-5, superdark 3 from days 3-6, etc.), resulting in a dark reference file for each day. This

yields a more accurate measurement of hot pixels around a given observation.

The procedural differences between the previous algorithm (which is described in Biretta and Bourque, 2014), and the new algorithm are illustrated graphically in Figures 10 and 11. More details of these new features as well as an outline of each step of the new algorithm is given below.

Gather RAW darks from anneal cycle

All available individual **_raw.fits* dark frames from the WFC3/UVIS Daily Monitor and WFC3/UVIS Anneal programs that were observed during a given anneal cycle are gathered. These are the individual frames that are used to construct the UVIS dark reference files.

CTE correct RAW darks

The individual dark frames are CTE corrected using the CTE correction algorithm (Anderson, 2013; code available at http://www.stsci.edu/hst/wfc3/tools/cte_tools, v0.1). As previously mentioned, the CTE correction helps to restore faint signal in hot pixels and cosmic rays that is otherwise lost due to CTE effects. It is important to note that this step of the algorithm is not used in the creation of non-CTE-corrected dark reference files; non-CTE-corrected reference files will continue to be generated and provided to the user community in order to calibrate non-CTE-corrected observations. Users are encouraged to only use CTE-corrected dark reference files to calibrate CTE-corrected science data, otherwise, the CTE trails that exist in non-CTE-corrected science data would not be properly subtracted during the dark calibration step in the CALWF3 calibration pipeline.

Subtract bias and postflash

The CTE corrected RAW darks are sent through the CALWF3 calibration pipeline in order to subtract the postflash signal (if the darks are postflashed) as well as the bias levels. This is achieved by setting the header keywords BIASCORR, BLEVCORR, and FLSHCORR to "PERFORM" in the individual frames. With BLEVCORR on, temporary **_blv_tmp.fits* files are created, which are bias-subtracted images with overscan regions trimmed. These files serve as the input files for cosmic ray rejection (Deustua et al., 2016, Section 2.1.1, Page 18).

Flag cosmic rays

For the CALWF3 processing described in the previous step, the CRCORR header keyword is also set to "PERFORM", which causes CALWF3 to perform cosmic ray rejection on the **_blv_tmp.fits* files. CALWF3 flags pixels affected by cosmic rays with a value of 8192 in the Data Quality (DQ) arrays of the files. The parameters that determine cosmic ray identification are defined in the cosmic-ray rejection parameter table (CRREJTAB), notably the

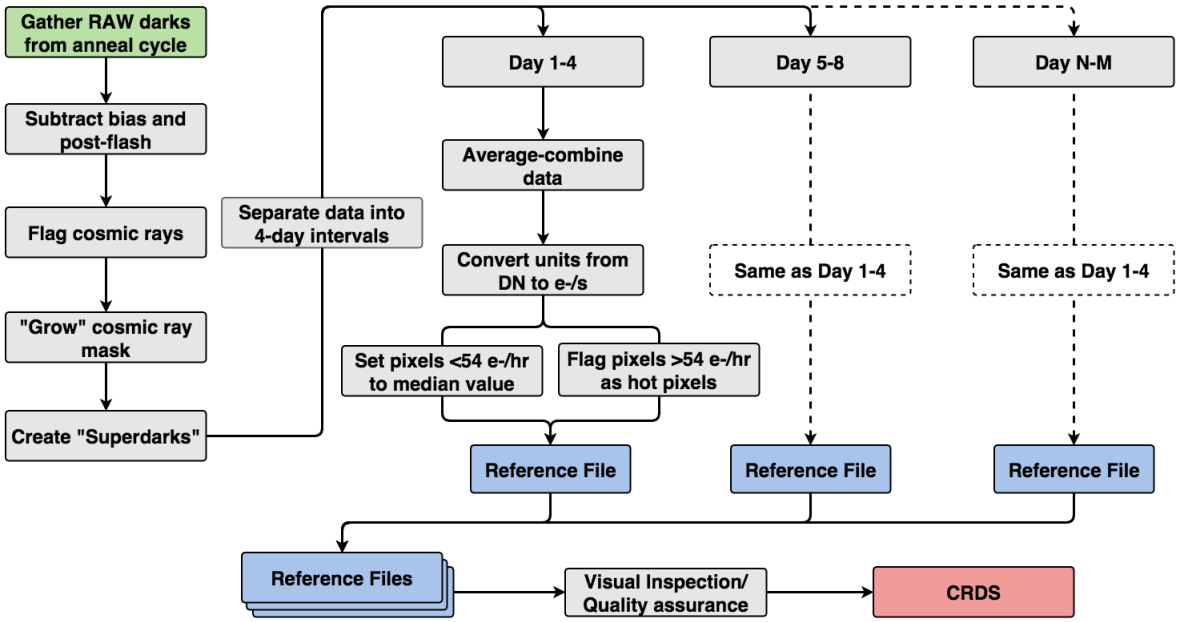

Fig. 10.—*The UVIS dark calibration pipeline for the old algorithm*

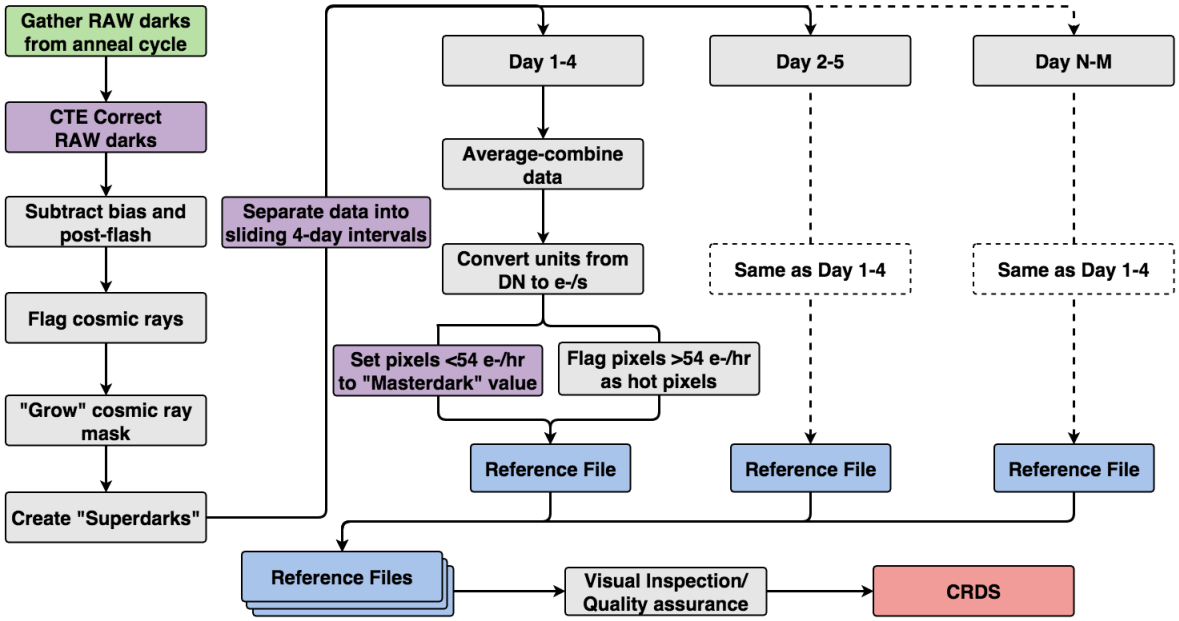

Fig. 11.—*The UVIS dark calibration pipeline for the new, improved algorithm. Magenta boxes represent major changes from the previous algorithm.*

CRSIGMAS (the rejection threshold), CRRADIUS (The radius (in pixels) for propagating cosmic ray), and CRTHRESH (propagation factor) parameters. For the UVIS dark pipeline, we use a custom CRREJTAB with parameters *CRSIGMAS=40,39,38*, *CRRADIUS=0.5*, and *CRTHRESH=0.5555*.

Grow cosmic ray mask

As a conservative measure to ensure that the wings of cosmic rays are properly flagged, we "grow" the flagged cosmic rays by a radius of 2 pixels in the **_blv_tmp.fits* files using the IRAF task *crgrow*. Figure 12 shows an example of this cosmic ray mask growth.

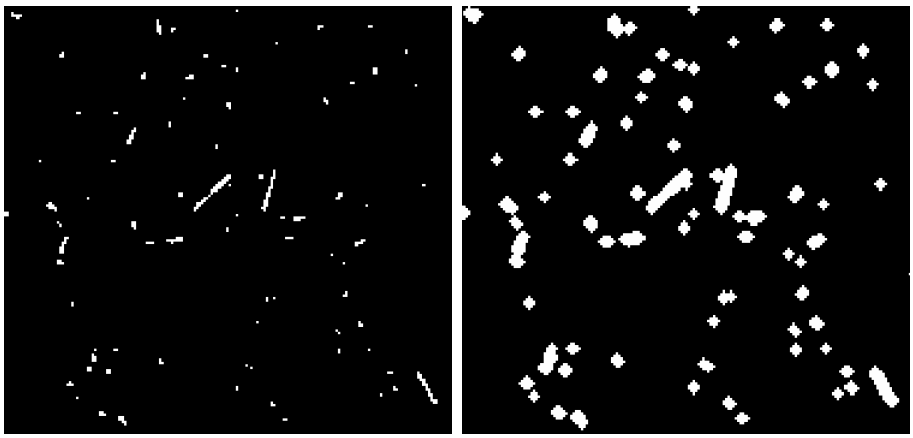

Fig. 12.—*An example of a zoomed-in region of a cosmic ray mask before (left) and after (right) the mask is grown.*

Create superdarks/Separate into sliding 4-day intervals

The CR-grown **_blv_tmp.fits* files are separated into groups of sliding 4-day "windows" based on the values of the EXPSTART keyword (i.e. the date and time of observation) in the individual frames; window 1 contains frames whose observations occurred between the earliest observation of the anneal cycle and four days after that; window 2 contains frames that occurred between (earliest observation + 1 day) and (earliest observation + 5 days); window 3 contains frames that occurred between (earliest observation + 2 days) and (earliest observation + 6 days), etc. Thus, each window usually contains between 7-15 individual frames, all of which were observed within a particular four-day period.

Average-combine data

For each window, the group of **_blv_tmp.fits* files are combined using the IRAF task *mscombine*. The *dqbits* parameter is set so that *mscombine* discards pixels that have a non-zero DQ value (i.e. the cosmic rays) during the average-combination. Furthermore, the *reject*

parameter is set to *"none"* so that no further rejection of pixels (beyond those discarded by *dqbits*) occurs, and the *combine* parameter is set to *"average"* so that the pixels are average-combined. The result is a "superdark" image (with an empty DQ array) for each window. It is also during this step that the USEAFTER header keyword is set in each superdark; the value of this keyword indicates the day and time after which science observations should use the particular dark reference file during calibration (i.e. the dark reference file should be used if the science observation's EXPSTART is greater than the USEAFTER).

Convert units from DN to e-/s

Since the individual RAW frames and corresponding *blv_tmp.fits* frames are in units of DNs (Data Number), so are the corresponding superdarks. However, since the CALWF3 calibration pipeline requires dark reference files to have units of electrons per second, the superdarks are multiplied by the gain and divided by the 900-second exposure time to convert the superdarks from units of DN to units of e-/s. The gain is multiplied to each amplifier individually, using the values from the header keywords ATODGNA, ATODGNB, ATODGNC, and ATODGND (all currently ∼1.56 e-/DN) for amps A, B, C, and D, respectively.

Set pixels <54 e-/hr to masterdark value

The pixel values in the superdarks represent the average dark current that the UVIS detector exhibited over a four-day timespan, and it is at this point that we can determine which pixels can be considered useable and which should be flagged as hot. To determine these two populations, the 54 e-/hr threshold is employed; pixels whose values are below this threshold are considered "good" and pixels whose values are above are considered hot.

In a separate routine, a "masterdark" is constructed by average-combining the individual dark frames from an entire anneal cycle, again using the IRAF task *mscombine*. Thus, the pixel values in the "masterdark" frame represent the average dark current over a ∼30 day timespan. Since the dark current only changes at a rate of ∼1 e-/hr/year, we believe that the dark current is sufficiently stable over a month timespan and thus the deeper masterdark provides a more accurate measurement of the dark current than a 4-day superdark. Therefore, we set each good pixel to its corresponding value in the masterdark image. Thus, unlike in the previous algorithm in which every good pixel was set to the same value (i.e. the frame's median value), each good pixel in the new algorithm has a unique value that reflects its own anneal-cycle-average dark current. However, since the masterdark uses individual dark frames from an entire anneal cycle, a masterdark cannot be constructed until an anneal cycle is completed, and so in order to create dark reference files within the current anneal cycle, we set the good pixels to values from the previous anneal cycle's masterdark. Again, we believe that the evolution of the dark current over a two month timespan is minimal and thus the previous anneal cycle's masterdark still provides an accurate measurement of the dark current.

However, there are two corner-cases in which the previous anneal cycle's masterdark cannot be used: (1) during the first anneal cycle of Cycle 17, when there was not enough previous data to construct a masterdark, and (2) during the first postflash-era anneal cycle (the 08/2012 anneal), since the previous data was not postflashed. The dark reference files from these two anneal cycles use masterdark values from their own anneal cycles.

Flag pixels >54 e-/hr as hot pixels

Pixels in the superdark whose values exceed the 54 e-/hr threshold are flagged as hot pixels and set with a value of 16 in the DQ array.

Visual inspection/Quality assurance

Superdarks from each 4-day window make up the set of dark reference files to be delivered to CRDS and used in the CALWF3 calibration pipeline. Before delivery, however, we visually and analytically inspect each reference file to ensure that they are of good quality. There are some notable criteria in which a dark reference file would be remade, or not be delivered entirely, namely:

1. *Too few input individual dark frames* - If a scheduling anomaly occurs in which only a few or no UVIS dark observations were acquired over a 4-day timespan, the dark reference file may not be delivered to CRDS. In this case, science observations that occurred during the corresponding 4-day window would use the reference file from the previous 4-day window.

2. *Corrupted input individual dark frames* - If one or more of the individual dark observations is somehow corrupted during nominal processing or transmission, the observation may be discarded or re-calibrated, and its corresponding dark reference file(s) may be recreated.

3. *Abnormally high median value in individual dark frames* - If one or more of the individual dark observations exhibits a median value exceeding 8 e-/s, the observation may be discarded, and its corresponding dark reference file(s) may be recreated. This occasionally occurred in early on-orbit observations due to light leaks, but has since been procedurally addressed (for further details, see the observing description of recent CCD Daily Monitoring programs, e.g. 14369).

Delivery to CRDS

All dark reference files that pass inspection are delivered to CRDS. At this time, the references files are renamed using the CRDS reference file naming convention (described further at http://www.stsci.edu/hst/observatory/crds/file_structure.html). It is important to note that the CTE-corrected dark reference files have a suffix of **_dkc.fits*, while the non-CTE-corrected files retain the nominal suffix of **_drk.fits*. Typically, the reference files become available to the user community within 7-10 days from the conclusion of the 4-day window.

Comparison Between Previous and New Algorithms

In this chapter, we seek to analyze and quantify the differences between the previous algorithm and the new algorithm. We begin the discussion by examining the pixel values of dark reference files generated using each algorithm. Figure 13 displays a histogram showing the distribution of non-hot pixel values across the full frame of the detector for a typical reference file. For the previous algorithm, all non-hot pixels are set to the median value of the frame, as represented by the dashed orange line. For the new algorithm, non-hot pixel values are set to the masterdark value for the given anneal cycle, and thus we see a normal distribution with a slight trail of positive dark current values, tapering off until the 54 e-/hr hot pixel threshold. Figure 13 reiterates that the values of the new dark reference files reflect actual dark current values for each pixel, not the median value across all pixels.

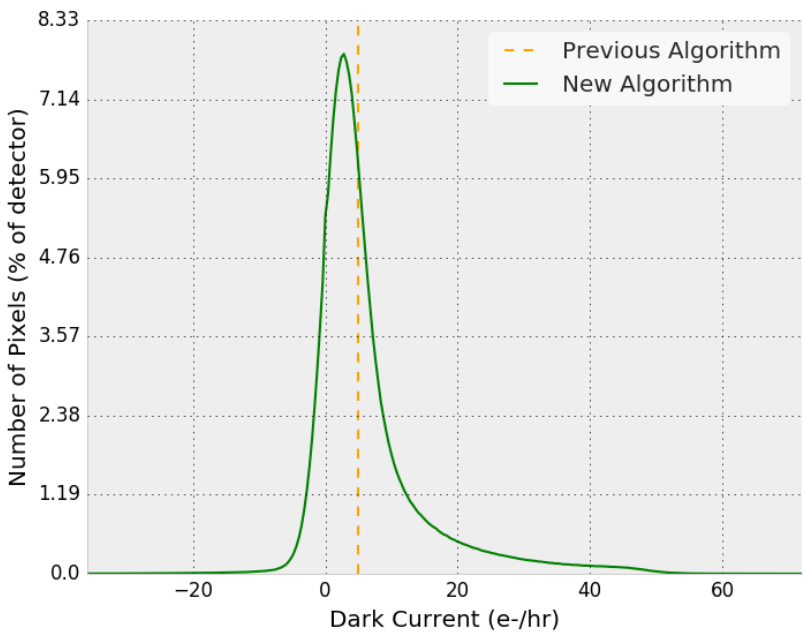

Fig. 13.—*A histogram of the 'good' (i.e. non-hot) pixel values present in a typical dark reference file created with the previous algorithm (orange) and with the new algorithm (green). Since the previous algorithm set all 'good' pixel values to the frame's median value, the pixels values of the previous-algorithm reference file do not have a distribution. Bin size is ∼0.4 e-/hr.*

Next, we analyze the number of hot pixels measured in previous reference files compared to that in the CTE-corrected reference files generated from the new algorithm, as plotted in Figure 14. The apparent difference between the two flavors is that more hot pixels are measured in the new reference files than the previous reference files, likely attributed to the CTE-correction present in the new algorithm; as mentioned previously, the CTE correction helps restore faint signal normally lost to CTE effects, and so more hot pixels are preserved

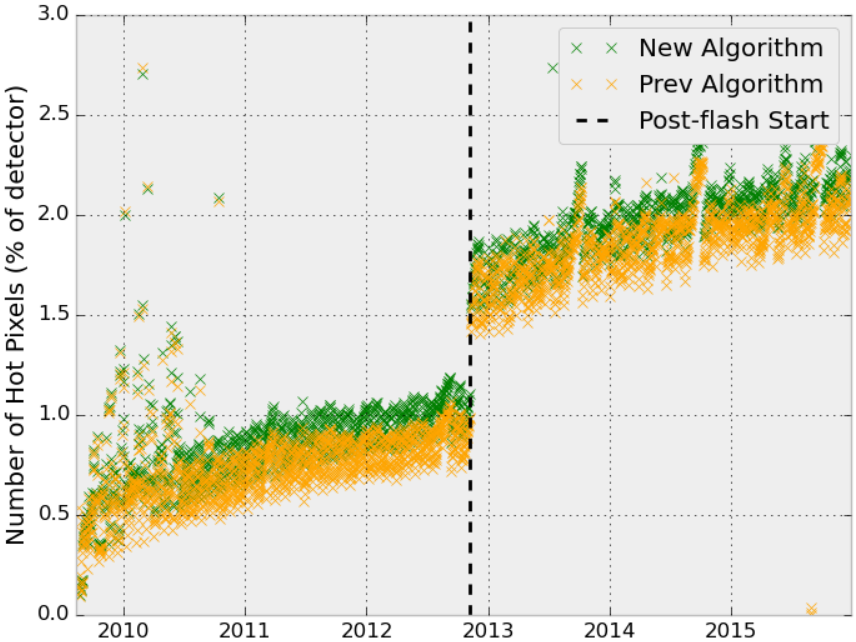

Fig. 14.—*The number of hot pixels present in dark reference files over time for darks generated from the previous algorithm (orange) and from the new algorithm (green). The dotted black line represents when dark observations began using postflash in November, 2012.*

and measured. Regardless, the new reference files show the same long-term trends that are seen in the previous darks, as expected.

It is interesting to note that Figure 14 reveals a discrepancy between the number of hot pixels counted in individual dark observations (as plotted in Figure 6) and those counted in the dark reference files (currently ∼4% versus ∼2%, respectively). The cause of this effect is currently unknown, though could likely be attributed to the average-combination of the individual dark frames when producing the reference files; pixels which are hot in only a few individual frames or barely exceed the hot pixel threshold would not skew the average sufficiently enough to push the pixel over the hot pixel threshold in the final averaged product.

Another significant difference between the previous and new algorithm is the use of the 'sliding' four-day window, which improves the flagging of hot pixels in science data. Table 2 illustrates how the sliding window affects the choice of dark reference files to use for calibration (i.e. the value of the DARKFILE header keyword). We use the individual dark files that make up a four-day window starting on 2015-09-13 as an example of observations that are acquired during a particular window (for illustration purposes only; dark frames are not calibrated with a dark reference file). In the case of the previous algorithm, each observation

Rootname	Observation Date	Prev. Reference File	USEAFTER	New Reference File	USEAFER
icqa0ymxq	2015-09-13 01:45:08	za117502i_drk.fits	2015-09-13 01:45:08	zcv15569i_drk.fits	2015-09-13 01:14:47
icqa0yn1q	2015-09-13 02:02:23	za117502i_drk.fits	2015-09-13 01:45:08	zcv15569i_drk.fits	2015-09-13 01:14:47
icqa0za9q	2015-09-14 00:50:09	za117502i_drk.fits	2015-09-13 01:45:08	zcv1556ai_drk.fits	2015-09-14 00:50:09
icqa0zafq	2015-09-14 01:07:24	za117502i_drk.fits	2015-09-13 01:45:08	zcv1556ai_drk.fits	2015-09-14 00:50:09
icqa1agaq	2015-09-14 22:21:31	za117502i_drk.fits	2015-09-13 01:45:08	zcv1556bi_drk.fits	2015-09-14 22:21:31
icqa1aglq	2015-09-14 22:38:46	za117502i_drk.fits	2015-09-13 01:45:08	zcv1556bi_drk.fits	2015-09-14 22:21:31
icqa1bkfq	2015-09-15 08:12:03	za117502i_drk.fits	2015-09-13 01:45:08	zcv1556bi_drk.fits	2015-09-14 22:21:31
icqa1bkjq	2015-09-15 08:44:13	za117502i_drk.fits	2015-09-13 01:45:08	zcv1556bi_drk.fits	2015-09-14 22:21:31
icqa1cnxq	2015-09-16 00:00:40	za117502i_drk.fits	2015-09-13 01:45:08	zcv1556ci_drk.fits	2015-09-16 00:00:40
icqa1co9q	2015-09-16 00:17:55	za117502i_drk.fits	2015-09-13 01:45:08	zcv1556ci_drk.fits	2015-09-16 00:00:40

Table 2:*The dark reference files applied to a given individual dark observation during a four-day window that begins on 2015-09-13.*

is calibrated with the same dark reference file (since previous-algorithm reference files are constructed from hard, non-sliding four-day windows), whereas for the new algorithm, which uses a sliding four-day window, four different dark reference files are applied over the course of the window.

Ideally, during the dark correction part of the calibration, the dark reference file will flag all hot pixels in the individual frames with a value of 16 in the DQ array, and thus the "good" pixels (i.e. the pixels with DQ values of 0) in the resulting **_flt.fits* files will be completely void of hot pixels. In reality, however, this is not the case, since the images that make up the four-day window are averaged together to form the dark reference file. Thus, observations that occur at the beginning of the four-day window may have pixels flagged that become hot 1-3 days later (i.e. too many hot pixels are flagged). Conversely, observations that occur towards the end of the four-day window may have recently-formed hot pixels that were not present during the 1-3 days prior, and thus are not flagged (i.e. too few hot pixels are flagged). Therefore, the calibrated files have 'leftover' (i.e. uncorrected) hot pixels that exist in the individual observations, but are not flagged in their corresponding dark reference file. The use of the sliding four-day window helps to mitigate the number of uncorrected hot pixels by providing dark reference files constructed from data that were acquired in the proceeding ∼4 days of a given observation; in this way, hot pixels are always flagged in a conservative manner.

Finally, we investigated the impact that the new dark reference files have on external science observations by performing differential aperture photometry of Omega Centauri observations. We measured the aggregate counts from a range of bright and faint stars using a 3-pixel radius aperture (with no distortion correction). We used two observations; one taken with the high-background wide-band F606W filter and one taken with the low-background narrow-band F673N filter, each calibrated using previous-algorithm darks as well as new-algorithm darks. The results are shown in Figure 15. The ratio of the counts between the two algorithms versus the counts from the observations calibrated with the previous algorithm reveal a 1% difference for stars with ∼1000 electrons and a >2% difference for stars

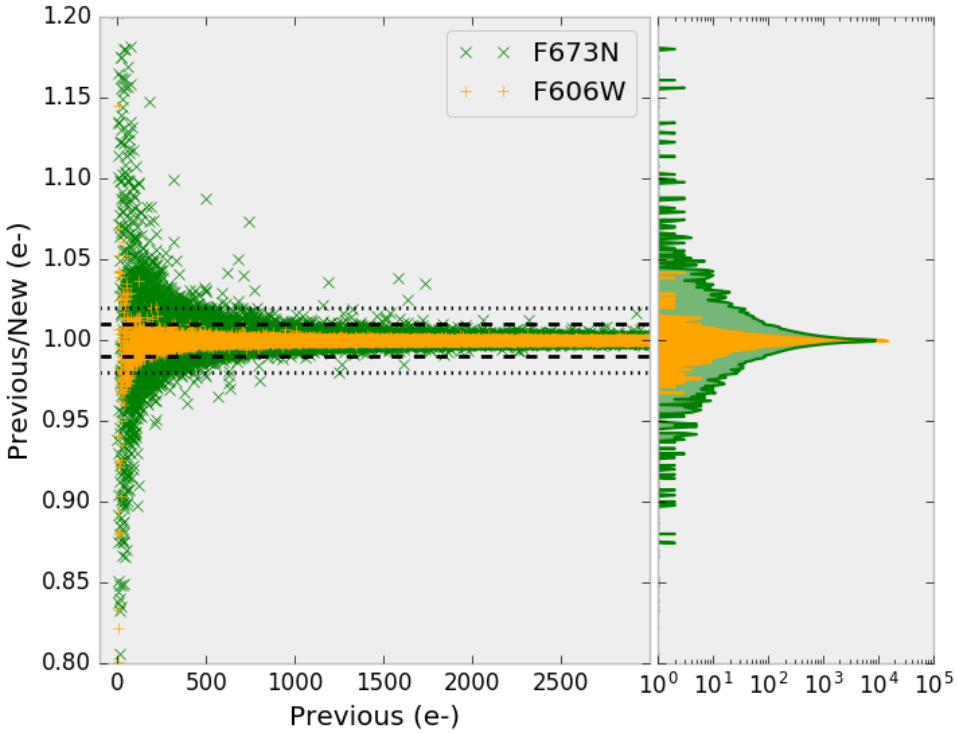

Fig. 15.—*Aperture photometry results of Omega Centauri, using 3-pixel radius, showing the ratio of counts obtained from sources calibrated with darks from the new algorithm over sources calibrated from the previous algorithm, versus the counts obtained using the previous algorithm. Results from two observations are plotted; one from a wide-band filter with high background (F606W, orange, dataset icqx12bmq) and one from a narrow-band filter with low background (F673N, green, dataset iben02iqq). Overplotted are lines showing 1% (dashed) and 2% (dotted) difference. The right panel contains a histogram showing the distribution of the ratio values (bin size is 0.0008).*

with less than $\sim$ 500 electrons in the low-background regime, while virtually all stars in the high-background regime experience a <1% difference. Thus, in this particular test, the new-algorithm darks only make a significant scientific impact on faint stars of <1000 electrons in low-background observations; we expect the net effect to be comparable on science observations under similar observing conditions.

Reprocessing of All On-orbit Dark Reference Files

With the release of the CALWF3 v3.3 calibration pipeline in February 2016, dark reference files generated using the improved algorithm have been re- delivered to the CRDS for all on-orbit data. As previously indicated, both CTE-corrected (**_dkc.fits*) and non-CTE-corrected (**_drk.fits*) dark reference files have been generated. Figure 16 shows the number

of dark reference files delivered to CRDS for both the previous and new algorithms since the beginning of Cycle 17 through the installation of CALWF3 v3.3. Approximately 1900 CTE-corrected reference files and 1900 non-CTE-corrected reference files (for a total of 3800 reference files) have been generated with the new algorithm and delivered to CRDS as of February 23rd, 2016.

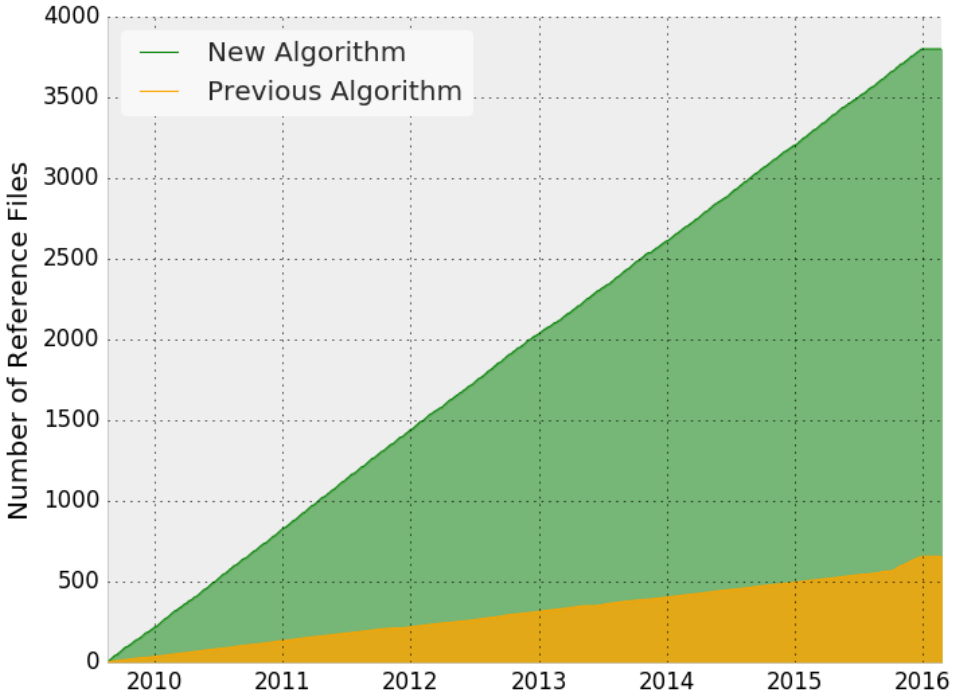

Fig. 16.—*The cumulative number of dark reference files delivered to CRDS from the start of Cycle 17 through the installation of calwf3 v3.3 (02/23/2016) for reference files generated from the new algorithm (green, 3800 total) and for reference files generated from the previous algorithm (orange, 656 total).*

Users can obtain data calibrated with the improved dark algorithm by simply re-retrieving from the MAST archive. Users wishing to manually re-calibrate can obtain the new dark reference files through the CRDS website (https://hst-crds.stsci.edu/).

Acknowledgements

We would like to thank Russell Ryan for his thorough review of this ISR. We would also like to thank Marc Rafelski for his useful insight and discussions on improving the dark calibration algorithm, as well as Linda Dressel for her suggestions relating to our solar activity analysis.

References

Anderson, J., "Instructions for Using the Alpha-Release of the WFC3/UVIS Pixel-based CTE Correction," February, 2013, available at http://www.stsci.edu/∼jayander/X/EXPORT_WFC3UV_CTE/wfc3cte_alpha.docx

Baggett, S., Bourque, M., Biretta, J., Wheeler, T., Hickey, D., and Swain, S., "Anomalous Monitor Results After the Aug 2012 Anneal," WFC3 Technical Instrument Report 2013-01, March, 2013.

Biretta, J., and Baggett, S., "WFC3 Post-Flash Calibration," WFC3 Instrument Science Report 2013-12, June, 2013.

Biretta, J., and Bourque, M., "WFC3 Cycle 19 & 20 Dark Calibration: Part I," WFC3 Instrument Science Report 2014-04, April, 2014.

Deustua, S., ed. 2016, "WFC3 Data Handbook", Version 4.0 (Baltimore: STScI).

McMaster, Biretta, et al. 2008, "WFPC2 Instrument Handbook," Version 10.0 (Baltimore: STScI).

National Oceanic and Atmospheric Administration (NOAA), 2016, "Sunspot Numbers (International)," available at http://www.ngdc.noaa.gov/stp/ space-weather/solar-data/solar-indices/sunspot-numbers/international/listings/.

Ryan, R., Deustua, S., Sosey, M., Anderson, J., Baggett, S., Bajaj, V., Bourque, M., Bowers, A., Dahlen, T., Durbin, M., Gosmeyer, C., Gunning, H., Khandrika, H., Mack, J., MacKenty, J., Martlin, C., Kozhurina-Platais, V., and Sabbi, E., "The Updated Calibration Pipeline for WFC3/UVIS: A Reference Guide to calwf3 (version 3.3)," WFC3 Instrument Science Report 2016-01, February, 2016.

Solar Influences Data Analysis Center (SIDC), 2016, "Monthly and smoothed sunspot number," available at http://www.sidc.be/silso/monthlyssnplot.

Appendix A

Below, we break down each UVIS CCD Monitoring program, detailing the visit structure. Note that, starting with the November 2012 anneal procedure, darks acquired from the anneal and daily monitor programs are generally postflashed (i.e. "flashed"); darks acquired before this time were generally non-postflashed (i.e. "unflashed"). There are a few exceptions around the time of the November 2012 anneal (e.g. the cycle 20 daily monitor programs) that acquired both flashed and unflashed biases and darks. Beyond the cycle 20 programs, unflashed biases and darks have been acquired through separate "unflashed Monitor" programs (i.e. 13559, 14005, 14371).

Program 11909 (same structure each day):

Each day:

Visit 1: 2 unflashed bias, 1 unflashed dark

Visit 2: 1 unflashed bias, 2 unflashed dark

Program 12342 (even/odd day cycle):

Even-numbered days:

Visit 1: 2 unflashed bias, 1 unflashed dark

Visit 2: 2 unflashed dark

Odd-numbered days:

Visit 3: 2 unflashed dark

Visit 4: 2 unflashed dark

Program 12689 (4-day/7-visit cycle):

Day 1:

Visit 1: 2 unflashed bias, 1 unflashed dark

Visit 2: 2 unflashed dark

Day 2:

Visit 3: 2 unflashed dark

Visit 4: 2 unflashed dark

Day 3:

Visit 5: 2 unflashed dark

Day 4:

Visit 6: 2 unflashed dark

Visit 7: 2 unflashed dark

Programs 13073, 13074 (4-day/12-visit cycle introducing postflash):

Day 1:

Visit 1: 2 flashed bias, 1 flashed dark

Visit 2: 2 flashed dark
Visit 3: 2 unflashed dark

Day 2:
Visit 4: 2 flashed dark
Visit 5: 2 flashed dark
Visit 6: 2 unflashed dark

Day 3:
Visit 7: 2 unflashed bias, 1 unflashed dark
Visit 8: 2 flashed dark
Visit 9: 2 unflashed dark

Day 4:
Visit 10: 2 flashed dark
Visit 11: 2 flashed dark
Visit 12: 2 unflashed dark

Programs 13075, 13076 (4-day/8-visit cycle with no unflashed darks):

Day 1:
Visit 1: 2 flashed bias, 1 flashed dark
Visit 2: 2 flashed dark

Day 2:
Visit 3: 2 flashed dark
Visit 4: 2 flashed dark

Day 3:
Visit 5: 2 unflashed bias, 1 flashed dark
Visit 6: 2 flashed dark

Day 4:
Visit 7: 2 flashed dark
Visit 8: 2 flashed dark

Programs 13556-58, 14002-04, 14368-70 (4-day/7-visit cycle, all-flashed):

Day 1:

Visit 1: 2 flashed bias, 1 flashed dark

Visit 2: 2 flashed dark

Day 2:

Visit 3: 2 flashed dark

Visit 4: 2 flashed dark

Day 3:

Visit 5: 2 flashed dark

Day 4:

Visit 6: 2 flashed dark

Visit 7: 2 flashed dark

Appendix B

We performed a linear fit of the monitoring data (shown in Figure 5) for both the pre-postflash and postflash epochs using the *polyfit* method of the *NumPy* package. The results are shown in Figure 17 as dashed cyan lines. In the pre-postflash epoch, this increase was ∼60 pixels/day for hot pixels and ∼1.4 e-/hr/year for dark current. In the postflash epoch, the increase is roughly ∼90 pixels/day for hot pixels and ∼0.7 e-/hr/year for dark current. However, recent data suggests that the slope of the dark current and number of hot pixels appears to be flattening; A linear fit to data that occurred after the October 10, 2014 anneal (shown in orange in Figure 17) suggests that the slope is ∼70 pixel/day and ∼0.4 e-/hr/year for hot pixels and dark current, respectively.

This flattening out of the dark current could be possibly attributed to solar activity; during periods of high solar activity, the increased number of solar flares help to produce a strong solar magnetic field that deflect galactic cosmic rays. Conversely, during a solar minimum, a weaker solar magnetic field allows more galactic cosmic rays to reach Earth's atmosphere (and thus it is more likely for UVIS dark exposures to experience cosmic rays). If such a correlation exists, we would expect to see suppressed increases to dark current during times of high solar activity. Such a correlation was seen in HST/ACS Wide-Field Planetary Camera 2 (WFPC2) data, as shown in Figure 18 (McMaster, Biretta, et al., 2008).

Recent solar activity data (shown in red in Figure 17 (NOAA, 2016)) shows that an approximately year long period of relatively high solar activity occurred in the 2014-2015 time frame, just before the start of the October 2014 flattening. However, the solar activity data from October 2014 onwards does not appear to agree with our this hypothesis; solar activity clearly trends downwards while dark current and hot pixel data continues to exhibit a flat trend. It is interesting to note, however, that the solar maximum that occurred during ∼2011-2015 was significantly weaker than previous solar maxima (particularly the one that WFPC2 experienced in ∼2000-2004), as evident in Figure 19 (SIDC, 2016), which shows the number of sunspots over the past several solar cycles. Perhaps this relatively weaker solar maximum is a reason why significant suppression of growing dark current trends is not seen in the UVIS monitoring data.

Another factor contributing to the obvious anti-correlation between the WFPC2 dark levels and solar maximum may be that the WFPC2 dark current overall was due to more than simply the thermal component arising within the detector itself. The WFPC2 CCD windows were constructed of MgF2, a substrate found on-orbit to luminesce in the presence of cosmic rays. This luminescence produced an additional substantial 'glow' in the WFPC2 dark frames. We speculate that the high dark current level on WFPC2, with the extra 'glow' component from the MgF2 window, served to accentuate the relationship between WFPC2 dark level and solar activity.

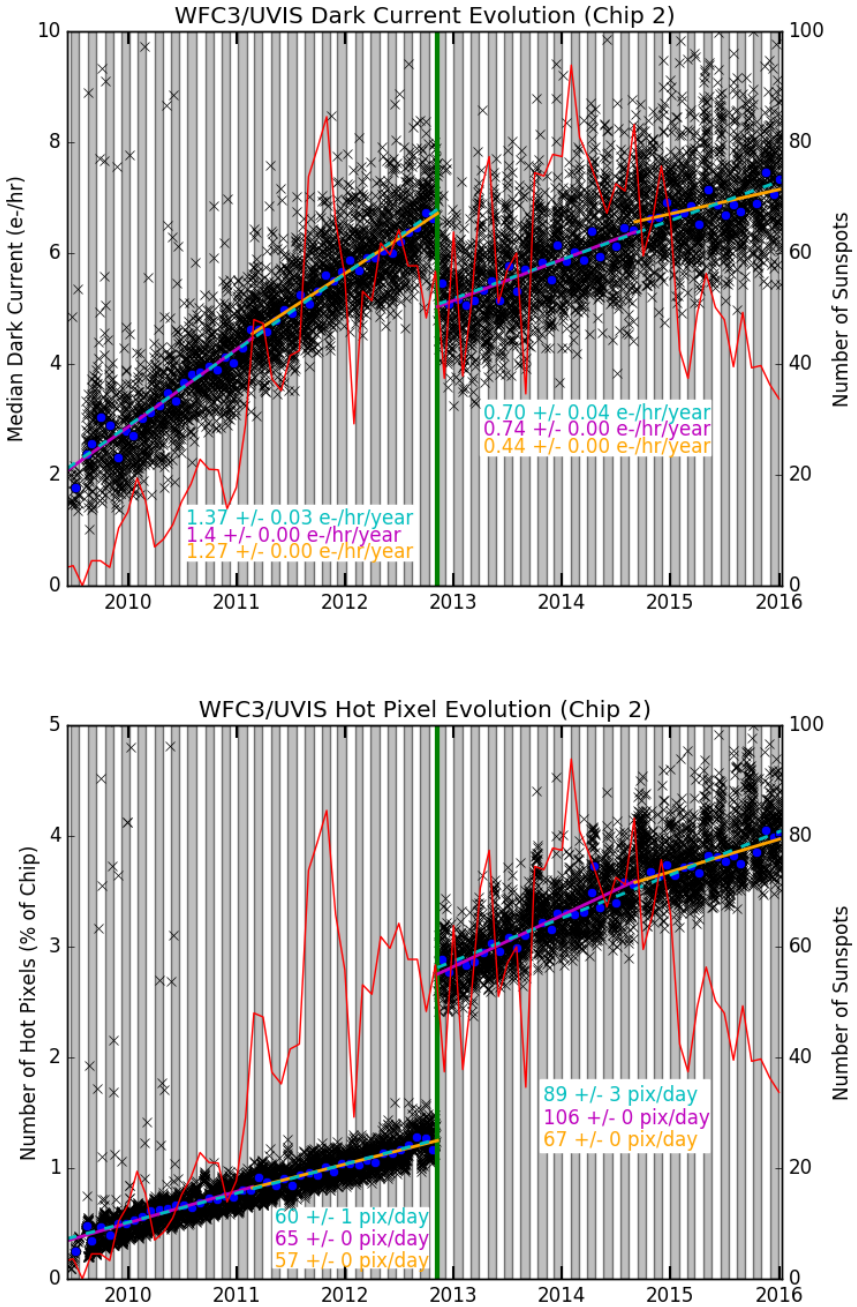

Fig. 17.—*The median dark current (top) and the number of hot pixels (bottom) over time for UVIS chip 2 (black data points). The blue dots represent the median value for each anneal cycle. Linear fits are overplotted and fit slopes are labeled; The dotted cyan line represents a linear fit for the pre-postflash and the postflash epochs, while the solid magenta and orange lines represent linear fits for data occurring in ∼2 year segments. For example, the magenta line in the postflash epoch represents a linear fit performed for data occurring after the October 10 2014 anneal procedure. Also overplotted are the number of sunspots (red) over the same time frame. Anneal cycles are shaded in gray/white intervals (i.e. gray/white boundaries represent anneal procedures). The postflash start date of November 08, 2012 is plotted in green.*

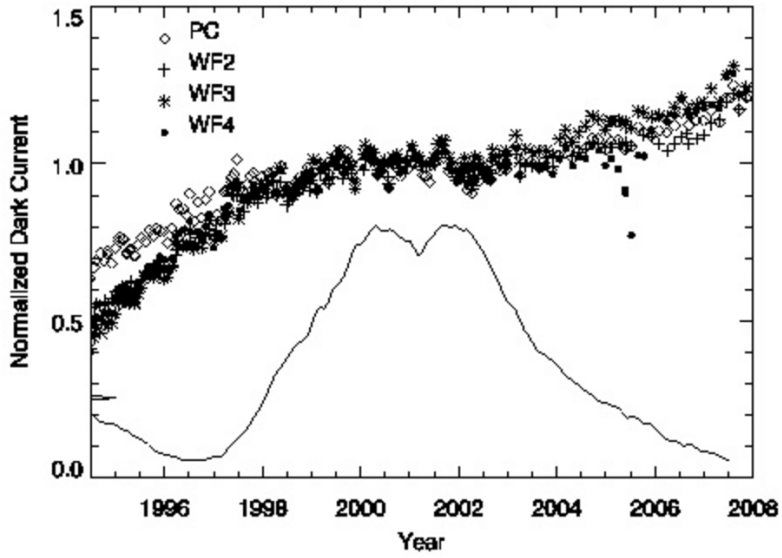

Fig. 18.—*The HST/ACS/WFPC2 dark current for all four detectors (scattered points) and the number of sunspots (solid line) over time. Data taken from the Cycle 17 WFPC2 Instrument Handbook, Section 4.8.2 (McMaster, Biretta, Et al., 2008).*

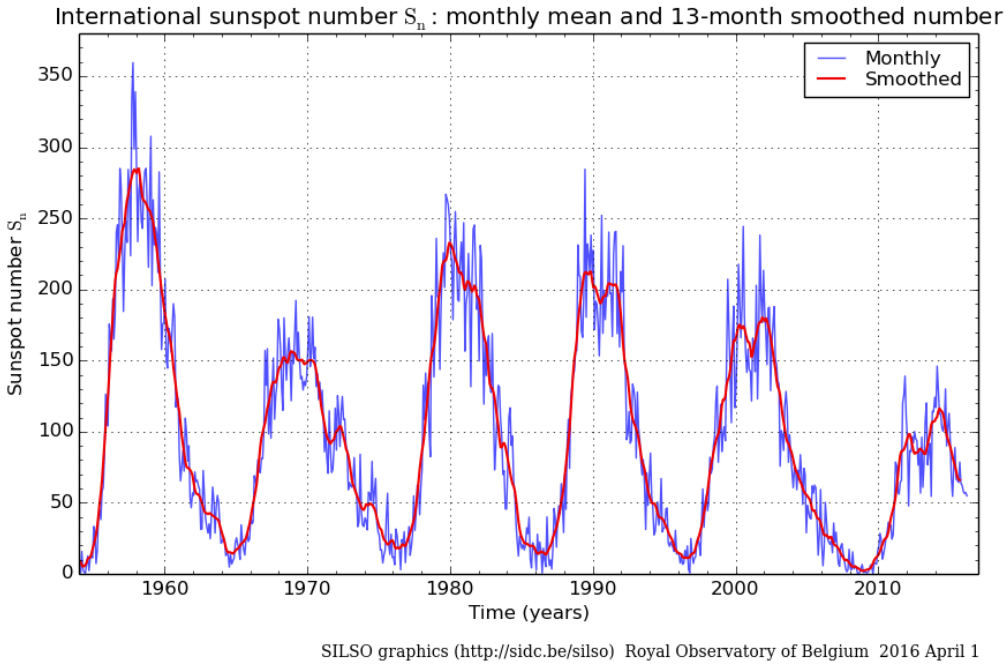

Fig. 19.—*The number of sunspots over the past several solar cycles. Data taken from SIDC, 2016.*